UNIVERSITY *of York*

This is a repository copy of *Direct Imaging of Kinetic Pathways of Atomic Diffusion in Monolayer Molybdenum Disulfide*.

White Rose Research Online URL for this paper:
https://eprints.whiterose.ac.uk/117124/

Version: Accepted Version

White Rose
university consortium
Universities of Leeds, Sheffield & York

eprints@whiterose.ac.uk
https://eprints.whiterose.ac.uk/

Direct imaging of kinetic pathways of atomic diffusion in monolayer molybdenum disulfide

Jinhua Hong, Yuhao Pan, Zhixin Hu, Danhui Lv, Chuanhong Jin, Wei Ji, Jun Yuan, and Ze Zhang

Just Accepted

Direct imaging of kinetic pathways of atomic diffusion in

monolayer molybdenum disulfide

Jinhua Hong[†, §, ¶], Yuhao Pan[‡, §], Zhixin Hu[‡], Danhui Lv[†], Chuanhong Jin[†, *], Wei Ji[‡, *],

Jun Yuan[†, ‖, *], Ze Zhang[†]

[†]*State Key Laboratory of Silicon Materials, School of Materials Science and Engineering,*

Zhejiang University, Hangzhou, Zhejiang 310027, China

[‡]*Beijing Key Laboratory of Optoelectronic Functional Materials & Micro-Nano Devices,*

Department of Physics, Renmin University of China, Beijing 100872, China

[‖]*Department of Physics, University of York, Heslington, York, YO10 5DD, United Kingdom*

[§] *These authors contributed equally to this work.*

**Direct observation of atomic migration both on and below surfaces is a
long-standing but important challenge in materials science as diffusion is one of
the most elementary processes essential to many vital material behaviors. Prob-
ing the kinetic pathways, including metastable or even transition states involved
down to atomic scale, holds the key to the underlying physical mechanisms. Here,
we applied aberration-corrected transmission electron microscopy (TEM) to
demonstrate direct atomic-scale imaging and quasi-real-time tracking of diffu-
sion of Mo adatoms and vacancies in monolayer MoS_2, an important 2D transi-
tion metal dichalcogenide (TMD) system. Preferred kinetic pathways and the
migration potential-energy landscape are determined experimentally and con-
firmed theoretically. The resulting three-dimensional knowledge of the atomic
configuration evolution reveals the different microscopic mechanisms responsi-
ble for the contrasting intrinsic diffusion rates for Mo adatoms and vacancies.
The new insight will benefit our understanding of material processes such as
phase transformation and heterogeneous catalysis.**

Key words: transition metal dichalcogenides, adatom and vacancy, surface migration,
energy landscape, single-atom tracking

Diffusion phenomena on surfaces and inside solids are important material processes closely associated with solid-state phase transformation[1], nanomaterials growth[2-4], single-atom doping[1] and heterogeneous catalysis[5]. To tailor or design these diffusion-related properties[6], it is essential to understand the underlying atomic process involved. However, the determination of microscopic mechanisms is non-trivial as diffusion can proceed along many different kinetic pathways. Even for simple self-diffusion inside solids, for example, it can take place via vacancy, interstitial or direct exchange mechanisms. Experimental determination of the stable and metastable configurations and their evolutions remains important to identify the dominant kinetic pathways involved, as well as providing vital realistic calibration to the complex *ab-initio* calculation.

Among the available experimental techniques, scanning tunneling microscopy (STM)[7, 8], atomic force microscopy (AFM)[9], and field ion microscopy (FIM)[10] have the required atomic resolution to image the surface migration of adatoms[11-15], and the rotation[16], transformation[9, 17, 18] and self-assembly[19] of adsorbate molecules. With the development of aberration correction optics, transmission electron microscopy (TEM) has been demonstrated as an alternative technique with a proper time window to observe adatom diffusion[20] or defect evolution[21-37]. However, the experimental single-atom tracking and statistical analysis of the metastable/intermediate states in atomic migration via different mechanisms are still limited. Furthermore, in contrast with the well-known one-dimensional pathway-dependent barrier, the two-dimensional potential landscape of the surface diffusion has never been mapped experimentally.

In this paper, we report a direct observation of the dynamics of bulk-like in-plane diffusion of Mo vacancies and surface migration of Mo adatoms in monolayer MoS_2, by atomic-scale tracking using chemically sensitive scanning transmission electron microscopy (STEM). As monolayer MoS_2 has a sandwich structure consisting of a Mo layer bonded by surface S layers on both sides, it is an ideal model system to study and contrast atom migration both on and below the surface. Specifically, we show that such observation can help identify the preferred migration pathway and

2

outline the two-dimensional migration energy landscape. *Ab-initio* density function theory (DFT) calculation further provides detailed quantum mechanical description of the atomic processes along such kinetic pathways, accounting for the different diffusion rates measured for adatoms and vacancies. As a member of transition metal dichalcogenides[38], MoS_2 has shown considerable potential in applications such as catalysis[39-43] and electrode materials for batteries[44, 45]. The insight gained can enhance our understanding and optimization of applications of such materials and the relevant systems involving mass transport under either electronic, chemical or ionic currents.

Results

The migration of Mo vacancy and its metastable state. Figure 1**a-d** shows the time-lapsed annular dark-field (ADF) images of the migrating Mo vacancy within monolayer MoS_2 at room temperature. According to the Z-contrast mechanism responsible for ADF-STEM imaging, it is easy to quantitatively assign the nature of lattice atoms and vacancy defects in monolayer MoS_2. The total duration of observation was sufficiently short that we did not detect additional loss of Mo or S atoms in this area of interest. Note that the vacancy diffusion is actually the motion of the neighboring Mo atom, highlighted with arrows in Fig. 1**a-c**. The vacancy migration in Fig. 1**a-c** went through an intermediate state (labeled as V'_{Mo}) and gives the clue to the kinetic pathway for the hopping of Mo vacancy from one site in the Mo sublattice to the next (Fig. 1**d**). More vacancy hopping examples can be found in Supplementary Fig.S1-2 and Animation1-3.

We have also analyzed the kinetic pathway of Mo vacancy migration by *ab-initio* DFT calculation, starting with the atomic geometries deduced from TEM observation. Figure.1**e-h** show DFT fully-relaxed atomic models associated with Fig.1**a-d**, in which the migrating Mo atom is emphasized in blue and purple. The overall agreement between the experimental images and those derived from the DFT calculations confirms the correct identification of three-dimensional structure of the most stable vacancy configuration V_{Mo} (Fig. 1**a**,**e**) and metastable state V'_{Mo} (Fig.1**b,f**).

Figure 2**a,b** show the statistical counts and dwell-times of different configurations of Mo vacancy (V_{Mo} and V'_{Mo}) observed during their migration. The dominating counts and longer dwell time of vacancies in the V_{Mo} state support the proposition that it is the ground-state configuration whereas V'_{Mo} is a metastable configuration. Our experimentally determined kinetic pathway (Fig.1**e-g**) for Mo vacancy migration is consistent with the most-favored pathway derived from *ab-initio* DFT calculation, after considering various possibilities, as shown in Fig.2**c** where the transition state (TS) and the energetics involved are also presented. The red arrows in Fig.2**c** indicate the motion of neighboring Mo atom (in blue) with the details shown in Fig. 2**d** (see also Supplementary Animation 4). The TS state has an energy of 2.9 eV relative to that of the most stable Mo vacancy state (V_{Mo}). The origin of such a high energy barrier is the unsaturated Mo-S bonds and reorganization of the bond length (Fig. 2**d**). On the other hand, the energy of the metastable state V'_{Mo} (local energy minimum in Fig.2**c**) is only 0.6 eV below that of the TS state, which explains the limited dwell time and observation frequency for the V'_{Mo} state. This probably also explains the slight distortion of lattice Mo atoms seen in the experimental images in Fig. 1 as the atomic configuration is more mobile in such a shallow potential well to be captured precisely. Nevertheless, both activation energies are higher than the background thermal energy, suggesting the migration processes seen in Fig. 1 is electron-beam assisted. This is similar to that found for vacancy hopping in graphene[31, 46]. Despite that, an analysis of the migration trajectories (Supplementary Fig.S3) indicates that the vacancy migration within Mo sublattice is without directional preference. The travel distance and displacement of Mo vacancy both follow the trend expected for the random walk of particles (Supplementary Fig.S4). This suggests that the effect of the electron beam is probably limited to boosting the mobilities of the atoms with high migration barriers.

The tracking of Mo adatoms and their metastable states. For comparison, Figure. 3**a-f** show a time-lapse sequential of ADF-STEM images indicating the migration of a Mo adatom on the surface of a monolayer MoS_2. The Mo adatom[47] can be easily

4

identified and this assignment is supported by additional simulation and analysis shown in Supplementary Fig.S5-6. More examples of adatom hopping are presented in Supplementary Fig.S7 and Animation 5-7.

After analyzing numerous Mo adatoms (over 500 cases), we identified three most-frequently observed configurations of Mo adatoms: on top of Mo sites (T_{Mo}), above the center of the hexagon or the hollow site (H), and on top of S sites (T_S), shown in Fig. 4**a**,**c**,**e**, respectively. The corresponding atomic models are shown in Fig. 4**b**,**d**,**f**, all based on experimentally suggested geometry and fully-relaxed by *ab-initio* calculation. Side views of these structures are presented in Supplementary Fig. S8. The image simulations (Supplementary Fig. S9) based on these structural models are in agreement with the experiments.

The statistical analysis of the observed adsorption states in Fig. 4**g** demonstrates that T_{Mo} is the most common adatom configuration, H and T_S are less common by comparison. Correspondingly, the dwell time of adatoms shown in Fig. 4**h** also indicates that T_{Mo} is more stable than H and T_S, although the differences in the counting statistics and the dwell times among T_{Mo}, H and T_S are smaller than those found in the case of Mo vacancy. Consistent with the experimental result, DFT calculations give their relative energy as 0, 0.33 and 0.99 eV for T_{Mo}, H and T_S, respectively. Accordingly, we regard T_{Mo} as the most stable state and H, T_S as metastable states. The presence of more than one metastable state for adatom migration is a reflection of the increased degree of freedom of adatoms compared with that of the in-plane vacancy diffusion. This illustrates the richness of the surface diffusional phenomena and necessity of determining the dominant kinetic pathway.

Ab-initio calculation confirms that the experimental most-favored kinetic pathways for Mo adatom migration follows a $T_{Mo1} \rightarrow H \rightarrow T_{Mo2}$ transition (red arrows shown in Fig.4**i** and observed in Supplementary Animation 5), with an initial energy barrier of 0.62eV. The energy barrier for the less-favored $T_{Mo} \rightarrow T_S$ transition is calculated to be 1.11eV by comparison (Supplementary Fig.S10 and Animation 8). The detailed structure evolution across the $T_{Mo1} \rightarrow H \rightarrow T_{Mo2}$ transition can be followed in Fig.4**j** where the migrating adatom is emphasized in blue (see also Supplementary

5

Animation 9)**.** Compared with Mo vacancy diffusion, the reduced energy barriers for surface adatom migration are related to the smaller structural relaxation (Supplementary Fig.S11) with breaking of at most only one Mo-S bond.

Although both MoS_2 and graphene surfaces are considered to be inert, the kinetic pathways for the adatoms are very different and depend on both the surface and the adatoms, indicating strong chemical adatom-surface interaction in both cases. For example, adatoms on graphite still migrate in a similar hexagonal lattice but they follow either $T_1{\rightarrow}B{\rightarrow}T_2$ (Au adatom), $H_1{\rightarrow}B{\rightarrow}H_2$ (Al or Cr) or $B_1{\rightarrow}B_2$ (C adatom) pathways[24, 48]. Here B stands for bridge sites above the center of C-C bonds. By contrast, the bridge-site adsorption on MoS_2 is not, even locally, a stable configuration for Mo adatoms. The preference for the $T_{Mo1}{\rightarrow}H{\rightarrow}T_{Mo2}$ pathway on MoS_2 surface is, we believe, due to the tendency of the d-electrons of the Mo adatom to form covalent bonds with the surface S in a triangular-prismatic or octahedral coordination[49]. This chemically-sensitive adatom diffusion may dominate the diffusion rate of intercalating ions in layered materials as battery electrodes[41].

Similar to the Mo vacancy case, the migration trajectory of Mo adatoms suggests that the migration jumps have no obvious directional preference (Supplementary Fig.S12). The travel distance and displacement of the hopping Mo adatom (Supplementary Fig.S4) is typical of random walk or Brownian motion of particles, suggesting the electron beam may help overcome the migration energy barriers.

Hopping statistics of defect migration and potential energy landscape. The Mo adatom hopping statistics can be visualized spatially in terms of the polar scatter diagram shown in Fig.5**a**. The red-star dots indicate the final sites of one-step adatom hopping from the initial site on Mo (coordinate origin), all superimposed on the hexagonal MoS_2 lattice. The radii of inscribed circles represent the range of the hopping steps that can be reached from the circle center. Most hoppings are between T_{Mo} and H, without directional preference. The density distribution of dots in this polar diagram reflects the two-dimensional potential landscape of a Mo adatom on monolayer MoS_2, as higher density means more stable atomic configuration. The density distri-

6

bution indeed coincides qualitatively with the theoretical adsorption potential diagram shown in Fig.5**b**. The T_{Mo}, H and T_S sites are all valleys in this potential-energy landscape, corresponding to the ground and metastable states, shown in Fig.4, respectively. The contrasting energy barriers between $T_{Mo}{\rightarrow}H$ (0.62 eV) and $T_{Mo}{\rightarrow}T_S$ (1.11 eV) indicate that the $T_{Mo}{\rightarrow}H$ transition should be the elementary hopping process in thermally activated atomic migration.

Similarly, polar scatter diagram in Fig.5**c** summarizes the hopping step distribution of Mo vacancies, where green triangles stand for the final sites of one-step hopping of Mo vacancy whose initial site is the origin. Compared with the surface adatom migration, the energy landscape is much simpler as V_{Mo} jumps only between Mo sublattice sites. Moreover, this stable migration within the Mo layer also has no directional preference, indicating a 2D random walk behavior.

One should note that as individual one-step migration of defects occurs in picosecond, the transfer process itself is too fast to capture 'in flight'. The possible much longer dwelling on the ground- or metastable-state sites allows us to capture different ground/metastable configurations. Hence, we consider the observed transition between two different states as one hopping step, much slower than the "ps" hopping dynamics. Based on the above analysis of the potential landscape for Mo adatoms, we interpret the observed long-range one-step jumps in Fig.5**a** as consisting of several $T_{Mo}{\rightarrow}H$ elementary hopping events. This is supported by the relative population of the jumping steps as shown in Fig.5**d**, based on an independent hopping model. Here the 'zero peak' represents those observations that adatoms remain at the same site or return to the same starting site. The first peak around 0.18 nm represents the transition from T_{Mo} to H (the elementary hopping), and the second peak is attributed to transition from T_{Mo1} to T_{Mo2} (two successive basic hopping), and the third peak is the result of second-nearest-neighboring hopping, as illustrated by the insets in Fig. 5**d**. They are compared with the theoretically-predicted relative probability distribution, where the relative probability ratio of the elementary hopping $T_{Mo}{\rightarrow}H$, nearest-neighboring-site hopping $T_{Mo1}{\rightarrow}H{\rightarrow}T_{Mo2}$, and second-nearest-neighboring-site hopping is 1: 2/3: 1/6 (red curve, see Supplementary Fig. S13 and Note 1 for details).

The calculated results agree well with the experiment except the discrepancy for peak 3 at 0.64 nm due to the limited counts for long-range jumps and the possible involvement of the less-favored $T_{Mo} \rightarrow T_S$ pathway.

Figure 5**e** shows the hopping step of Mo vacancy. The vacancy has a much lower possibility to migrate in comparison with the case of adatom hopping, due to its much higher energy barrier. Nearest-neighboring vacancy hopping is responsible for the first peak and the second-nearest neighboring hopping contributes to the second peak (see inset pictures).

Discussion

For adatom surface migration, the structural evolution give rise to novel electronic properties, worth exploring by DFT calculation. We discover that certain adatom configurations (ground state T_{Mo} and metastable state H, T_S) all have magnetic moments >2 μ_B (Supplementary Fig.S14). They are all highly spin-polarized and localized mainly on Mo adatom, with a minor contribution from the neighboring S atoms. The significant density of states (mostly from the adatom's d orbitals) at Fermi levels may play an essential role in the physical properties of MoS_2, such as defect magnetism and reactivity as a catalyst.

The very different magnitudes of the energy barriers for Mo adatoms and vacancies can be ascribed to their contrasting microscopic diffusion mechanisms. In surface diffusion, adatoms not only relax more easily into the vacuum, but also retain the largest number of unbroken Mo-S bonds. A Mo adatom starts with three Mo-S bonds in the triangular-prismatic coordination as the most stable state[49] at T_{Mo} site, to two Mo-S bonds when going through a S-S bridge site, then to three Mo-S bonds in octahedral coordination[49] (H site) which is less energetically favorable. In the vacancy diffusion, Mo's migration within the confined Mo atom layer involves the breaking and reconnection of more covalent Mo-S bonds (Fig.2**d**): from initial Mo site (most-stable with six Mo-S bonds), through a S-S bridge site (two short Mo-S bonds with the 'Klein'-like S atoms, two long and weak Mo-S bonds with the 'zig-zag'-like

S atoms, Supplementary Fig. S11b), to a hollow-like site (metastable with six Mo-S bonds).

Finally, the observation of vacancy hopping and metastable adatom T_S, with energy barriers much higher than the thermal energy available, is a sign that the migration is influenced or even driven by the electron beam. Hence it is necessary to quantify the beam induced effect. Considering elastic knock-on scattering mechanism (Supplementary Fig. S15, 16), we conclude that the vacancy migration is induced solely by the electron beam and adatom migration is influenced by both thermal activation and beam-atom interaction. Fortunately, the beam-atom interaction allows us to explore more comprehensively different kinetic pathways, especially for vacancy dynamics inaccessible by thermal activation at a "safe" temperature. One may also note the slight atomic distortion of the lattice Mo below the migrating Mo in the vacancy hopping in Fig.1, which can be interpreted as a temporary displacement resulted from the electron beam radiation on the shallow potential landscape shown above. In the future studies, it would be very interesting to carry out *in-situ* TEM observation at variable temperatures and with higher temporal resolution, which would allow us to capture more precisely the atomic dynamics and determine quantitatively the migration kinetics experimentally, as a complement to DFT calculations.

In summary, we have demonstrated an efficient survey of the migration energy landscape using single-atom tracking and *ab-initio* calculation, providing a successful paradigm for exploration of the microscopic mechanisms of atom diffusion in solids. Its application in monolayer MoS_2 reveals the two-dimensional Mo diffusions on and below surface with very different covalent bonds reorganization along their preferred kinetic pathway. The results from our joint experiment-theory approach should be useful in the rational design of practical applications of TMDs, such as catalysts and ion intercalation in electrodes for batteries, as well as bringing us a new perspective on solid state mass transport in general.

During the review of this work, we noticed another work focused on the migration of single Pt atoms in MoS_2 monolayer[56].

Methods

Sample preparation Monolayer molybdenum disulfide was prepared onto silicon substrate with a 300-nm-thick oxide capping layer through standard mechanical exfoliation from bulky MoS_2 single crystals (SPI Supplies Inc.) using scotch tapes. Selected atomically thin samples were then transferred onto TEM grids and annealed at 200°C in vacuum (10^{-4} Pa) to remove surface residues and contaminations before loading into the TEM chamber.

ADF-STEM characterization ADF-STEM imaging was carried out in a FEI Titan ChemiSTEM microscope equipped with a probe corrector and operated at 200 kV. The probe current was set to be about 60 pA and the convergence angle to 22 mrad. The collection angle of the ADF-STEM detector was adjusted to 50~200 mrad. Time lapsed ADF-STEM images were recorded in three seconds interval with a frame size of 512×512 pixels (corresponding to 10×10 nm^2) and a pixel dwell time of 10 μs. The total electron dose to the specimen for each frame was estimated to be $9.7×10^6$ e^-/nm^2. ADF-STEM images were analyzed after a drift correction and Wiener filtering for a better signal-to-noise (S/N) ratio (Supplementary Fig. S17). All the observations were carried out at room temperature.

ADF-STEM image simulations, as shown in the Supplementary Fig. S9, were achieved by QSTEM[50] with the simulation parameters (the convergence and acceptance angles, the probe size) kept almost the same as those used experimentally.

Further analysis including the population, the duration time (or lifetime), and hopping step statistics were performed based on the raw ADF-STEM images recorded from clean regions of MoS_2 monolayers.

DFT calculations.

Density functional theory calculations were performed using the generalized gradient approximation for the exchange-correlation potential, the projector augmented wave

10

method[51] and a plane-wave basis set as implemented in the Vienna *ab-initio* simulation package (VASP)[52]. The energy cutoff for plane wave was set to 300 eV for structural relaxation and increased to 600 eV for total energy calculations. Dispersion correction was made at the van der Waals density functional (vdW-DF) level, with the optB86b functional for the exchange potential[53]. An 8×8 slab of monolayer MoS_2 with a 15Å vacuum layer perpendicular to the atomic plane was employed in all calculations to minimize the interactions between a defect and its images. All atoms in the supercell were allowed to relax until the residual force per atom was less than 0.01 $eV \cdot Å^{-1}$. Barriers of different diffusion pathways were revealed by the nudged elastic band (NEB) method[54]. The climbing-image technique[55] was used to precisely identify the transition state and the barrier height.

Potential landscape. The two-dimensional potential landscape of the adatom was calculated as follows. We first mapped 25 adsorption sites onto one third of the lattice hexagon, with equal spacing in the atomic plane (xy plane). A Mo adatom was put at these sites with its x, y coordinates fixed and z coordinates free to relax. Given the minimum energies at those sites, we extrapolate the energies into the whole hexagon to yield a continuous two-dimensional projected potential.

ASSOCIATED CONTENT

Supporting information: Including Supplementary Figures 1-19 and Notes 1, 2. This material is available free of charge via the internet at http://pubs.acs.org.

AUTHOR INFORMATION

Corresponding Authors

*Correspondence and request for materials should be addressed to C.J. (chhjin@zju.edu.cn), W.J. (wji@ruc.edu.cn) or J.Y. (jun.yuan@york.ac.uk).

Author contributions

J.H. and Y.P. contributed equally to this work. C.J., W.J. and J.Y. conceived the research. J.H. and D.L. contributed to the sample preparations. J.H., C.J., and J.Y. did the STEM characterizations,

REFERENCES

1.   Lin, Y. C.; Dumcencon, D. O.; Huang, Y. S.; Suenaga, K. *Nat. Nanotechnol.* **2014,** 9, 391-396.

2.   Hannon, J. B.; Kodambaka, S.; Ross, F. M.; Tromp, R. M. *Nature* **2006,** 440, 69-71.

3.   Hofmann, S.; Csanyi, G.; Ferrari, A. C.; Payne, M. C.; Robertson, J. *Phys. Rev. Lett.* **2005,** 95,036101.

4.   Jensen, L. E.; Bjork, M. T.; Jeppesen, S.; Persson, A. I.; Ohlsson, B. J.; Samuelson, L. *Nano Lett.* **2004,** 4, 1961-1964.

5.   Satterfield, C. N., *Mass transfer in heterogeneous catalysis*. (The MIT Press, 1970).

6.   Mantina, M.; Wang, Y.; Arroyave, R.; Chen, L. Q.; Liu, Z. K.; Wolverton, C. *Phys. Rev. Lett.* **2008,** 100, 215901.

7.   Bollinger, M. V.; Lauritsen, J. V.; Jacobsen, K. W.; Norskov, J. K.; Helveg, S.; Besenbacher, F. *Phys. Rev. Lett.* **2001,** 87, 196803.

8.   Kibsgaard, J.; Lauritsen, J. V.; Laegsgaard, E.; Clausen, B. S.; Topsoe, H.; Besenbacher, F. *J. Am. Chem. Soc.* **2006,** 128, 13950-13958.

9.   de Oteyza, D. G.; Gorman, P.; Chen, Y. C.; Wickenburg, S.; Riss, A.; Mowbray, D. J.; Etkin, G.; Pedramrazi, Z.; Tsai, H. Z.; Rubio, A.; Crommie, M. F.; Fischer, F. R. *Science* **2013,** 340, 1434-1437.

10. Tsong, T. T. *Phys. Today* **1993,** 46, 24-31.

11. Pedersen, M. O.; Osterlund, L.; Mortensen, J. J.; Mavrikakis, M.; Hansen, L. B.; Stensgaard, I.; Laegsgaard, E.; Norskov, J. K.; Besenbacher, F. *Phys. Rev. Lett.* **2000,** 84, 4898-4901.

12

12. Schaub, R.; Wahlstrom, E.; Ronnau, A.; Laegsgaard, E.; Stensgaard, I.; Besenbacher, F. *Science* **2003,** 299, 377-379.

13. Lo, R. L.; Hwang, I. S.; Ho, M. S.; Tsong, T. T. *Phys. Rev. Lett.* **1998,** 80, 5584-5587.

14. Brune, H.; Wintterlin, J.; Behm, R. J.; Ertl, G. *Phys. Rev. Lett.* **1992,** 68, 624-626.

15. Wang, K. D.; Zhang, C.; Loy, M. M. T.; Xiao, X. D. *Phys. Rev. Lett.* **2005,** 94, 036103.

16. Gao, L.; Liu, Q.; Zhang, Y. Y.; Jiang, N.; Zhang, H. G.; Cheng, Z. H.; Qiu, W. F.; Du, S. X.; Liu, Y. Q.; Hofer, W. A.; Gao, H. J. *Phys. Rev. Lett.* **2008,** 101, 197209.

17. Shi, D. X.; Ji, W.; Yang, B.; Cun, H. Y.; Du, S. X.; Chi, L. F.; Fuchs, H.; Hofer, W. A.; Gao, H. J. *J. Phys. Chem. C* **2009,** 113, 17643-17647.

18. Cheng, F.; Ji, W.; Leung, L.; Ning, Z. Y.; Polanyi, J. C.; Wang, C. G. *ACS Nano* **2014,** 8, 8669-8675.

19. Maksymovych, P.; Sorescu, D. C.; Yates, J. T. *Phys. Rev. Lett.* **2006,** 97, 146103.

20. Lin, Y. C.; Dumcenco, D. O.; Komsa, H. P.; Niimi, Y.; Krasheninnikov, A. V.; Huang, Y. S.; Suenaga, K. *Adv. Mater.* **2014,** 26, 2857-2861.

21. Komsa, H.-P.; Kurasch, S.; Lehtinen, O.; Kaiser, U.; Krasheninnikov, A. V. *Phys. Rev. B* **2013,** 88, 035301; Oh, S. H.; Benthem, K. v.; Molina, S. I.; Borisevich, A. Y.; Luo, W.; Werner, P.; Zakharov, N. D.; Kumar, D.; Pantelides, S. T.; Pennycook, S. J. *Nano Lett.* **2008,** 8, 1016-1019.

22. Lehtinen, O.; Kurasch, S.; Krasheninnikov, A. V.; Kaiser, U. *Nat. Commun.* **2013,** 4, 2098.

23. Lee, J.; Zhou, W.; Pennycook, S. J.; Idrobo, J. C.; Pantelides, S. T. *Nat. Commun.* **2013,** 4, 1650.

24. Lehtinen, P. O.; Foster, A. S.; Ayuela, A.; Krasheninnikov, A.; Nordlund, K.; Nieminen, R. M. *Phys. Rev. Lett.* **2003,** 91, 017202.

25. Kurasch, S.; Kotakoski, J.; Lehtinen, O.; Skakalova, V.; Smet, J.; Krill, C. E.; Krasheninnikov, A. V.; Kaiser, U. *Nano Lett.* **2012,** 12, 3168-3173.

26. Gan, Y. J.; Sun, L. T.; Banhart, F. *Small* **2008,** 4, 587-591; Girit, Ç. Ö.; Meyer, J. C.; Erni, R.; Rossell, M. D.; Kisielowski, C.; Yang, L.; Park, C.-H.; Crommie, M.; Cohen, M. L.; Louie, S. G. *Science* **2009,** 323, 1705-1708.

27. Zhang, W.; Sun, L. T.; Xu, Z. J.; Krasheninnikov, A. V.; Huai, P.; Zhu, Z. Y.; Banhart, F. *Phys. Rev. B* **2010,** 81, 125425.

28. Cretu, O.; Krasheninnikov, A. V.; Rodriguez-Manzo, J. A.; Sun, L. T.; Nieminen, R. M.; Banhart, F. *Phys. Rev. Lett.* **2010,** 105, 196102.

29. Nakada, K.; Ishii, A. *Solid State Commun.* **2011,** 151, 13-16.

30. Krasheninnikov, A. V.; Nordlund, K.; Lehtinen, P. O.; Foster, A. S.; Ayuela, A.; Nieminen, R. M. *Phys. Rev. B* **2004,** 69, 073402.

31. Kotakoski, J.; Mangler, C.; Meyer, J. C. *Nat. Commun.* **2014,** 5, 3991.

32. Robertson, A. W.; Allen, C. S.; Wu, Y. A.; He, K.; Olivier, J.; Neethling, J.; Kirkland, A. I.; Warner, J. H. *Nat. Commun* **2012,** 3, 1144.

33. Wang, W. L.; Santos, E. J. G.; Jiang, B.; Cubuk, E. D.; Ophus, C.; Centeno, A.; Pesquera, A.; Zurutuza, A.; Ciston, J.; Westervelt, R.; Kaxiras, E. *Nano Lett.* **2014,** 14, 450-455.

34. Warner, J. H.; Margine, E. R.; Mukai, M.; Robertson, A. W.; Giustino, F.; Kirkland, A. I. *Science* **2012,** 337, 209-212.

35. Ishikawa, R.; Mishra, R.; Lupini, A. R.; Findlay, S. D.; Taniguchi, T.; Pantelides, S. T.; Pennycook, S. J. *Phys. Rev. Lett.* **2014,** 113, 155501.

36. Lin, J.; Pantelides, S. T.; Zhou, W. *ACS Nano* **2015,** 9, 5189-5197.

37. Wang, S.; Lee, G.-D.; Lee, S.; Yoon, E.; Warner, J. H. *ACS Nano* **2016,** 10, 5419-5430.

13

38. Wang, Q. H.; Kalantar-Zadeh, K.; Kis, A.; Coleman, J. N.; Strano, M. S. *Nat. Nanotechnol.* **2012,** 7, 699-712.

39. Norskov, J. K.; Bligaard, T.; Rossmeisl, J.; Christensen, C. H. *Nat. Chem.* **2009,** 1, 37-46.

40. Hinnemann, B.; Moses, P. G.; Bonde, J.; Jorgensen, K. P.; Nielsen, J. H.; Horch, S.; Chorkendorff, I.; Norskov, J. K. *J. Am. Chem. Soc.* **2005,** 127, 5308-5309.

41. Gao, M. R.; Liang, J. X.; Zheng, Y. R.; Xu, Y. F.; Jiang, J.; Gao, Q.; Li, J.; Yu, S. H. *Nat. Commun.* **2015,** 6, 5982.

42. Sun, X.; Dai, J.; Guo, Y. Q.; Wu, C. Z.; Hu, F. T.; Zhao, J. Y.; Zeng, X. C.; Xie, Y. *Nanoscale* **2014,** 6, 8359-8367.

43. Xie, J. F.; Zhang, H.; Li, S.; Wang, R. X.; Sun, X.; Zhou, M.; Zhou, J. F.; Lou, X. W.; Xie, Y. *Adv. Mater.* **2013,** 25, 5807.

44. Liu, H.; Su, D. W.; Zhou, R. F.; Sun, B.; Wang, G. X.; Qiao, S. Z. *Adv. Energy Mater.* **2012,** 2, 970-975.

45. Li, W. F.; Yang, Y. M.; Zhang, G.; Zhang, Y. W. *Nano Lett.* **2015,** 15, 1691-1697.

46. Lee, G. D.; Wang, C. Z.; Yoon, E.; Hwang, N. M.; Kim, D. Y.; Ho, K. M. *Phys. Rev. Lett.* **2005,** 95, 205501.

47. Zhou, W.; Zou, X. L.; Najmaei, S.; Liu, Z.; Shi, Y. M.; Kong, J.; Lou, J.; Ajayan, P. M.; Yakobson, B. I.; Idrobo, J. C. *Nano Lett.* **2013,** 13, 2615-2622.

48. Hardcastle, T. P.; Seabourne, C. R.; Zan, R.; Brydson, R. M. D.; Bangert, U.; Ramasse, Q. M.; Novoselov, K. S.; Scott, A. J. *Phys. Rev. B* **2013,** 87, 195430.

49. Chhowalla, M.; Shin, H. S.; Eda, G.; Li, L. J.; Loh, K. P.; Zhang, H. *Nat. Chem.* **2013,** 5, 263-275.

50. Koch, C. T. QSTEM (2010); Koch, C.T. Determination of core structure periodicity and point defect density along dislocations. (Ph.D thesis, Arizona State University 2002).

51. Blochl, P. E. *Phys. Rev. B* **1994,** 50, 17953-17979.

52. Kresse, G.; Furthmuller, J. *Phys. Rev. B* **1996,** 54, 11169-11186.

53. Klimes, J.; Bowler, D. R.; Michaelides, A. *Phys. Rev. B* **2011,** 83, 195131.

54. Henkelman, G.; Jonsson, H. *J. Chem. Phys.* **2000,** 113, 9978-9985.

55. Henkelman, G.; Uberuaga, B. P.; Jonsson, H. *J. Chem. Phys.* **2000,** 113, 9901-9904.

56. Li, H.; Wang, S.; Sawada, H.; Han, G. G.; Samuels, T.; Allen, C. S.; Kirkland, A. I.; Grossman, J. C.; Warner, J. H. *ACS Nano* **2017,** 11, 3392-3403.
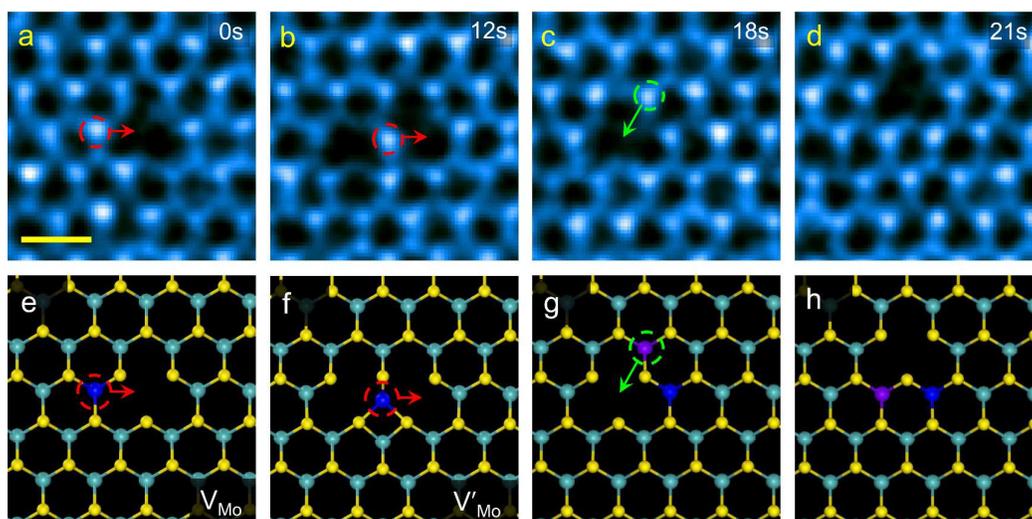
14

Figure 1. Atomic-scale migration of vacancy defects. (**a-d**) Time-lapse series of experimental ADF images of a Mo vacancy. Scale bar: 0.5nm. (**e-h**) DFT-relaxed atomic structures corresponding to the evolution in **a-d** from the Mo vacancy (V_{Mo} in **a**) to its metastable state (V'_{Mo} in **b**) and then to another Mo vacancy V_{Mo} in **c**. Scale bar: 0.5nm. Note the vacancy migration is actually the motion of a neighboring Mo atom, shown in blue or purple.
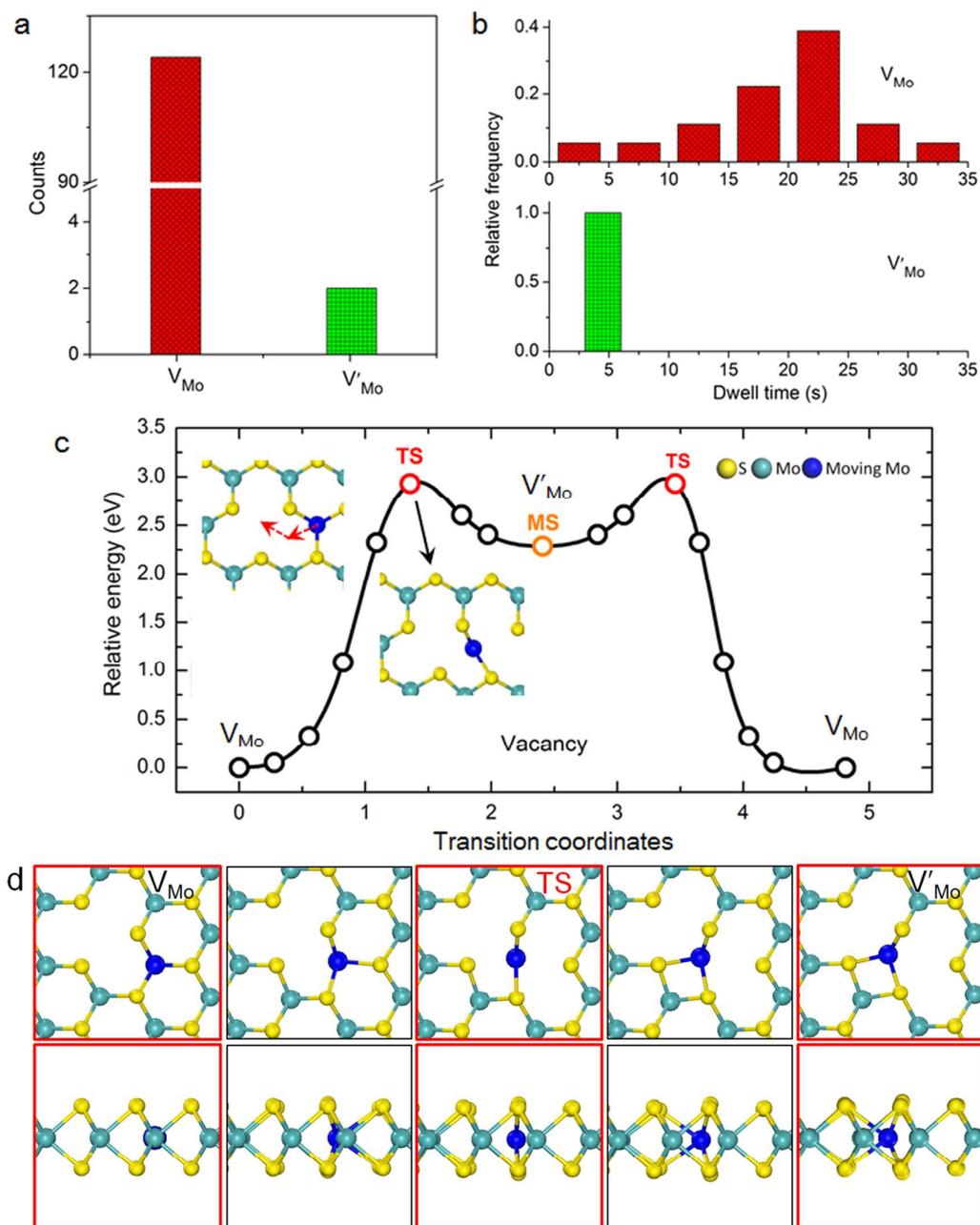
Figure 2. States of vacancy and their evolution. (**a-b**) Statistical counts and dwell time of vacancies and their metastable states during the migration of a Mo vacancy. (**c**) DFT calculated migration pathway of Mo vacancy. The dynamic process is shown by the inset atomic models with arrows illustrating the migration pathway of the neighboring Mo atom. (**d**) Detailed atomic dynamics of Mo vacancy migration with top-view and side-view, respectively. Note the $V_{Mo} \rightarrow V'_{Mo} \rightarrow V_{Mo}$ transition in **c** is symmetric, hence only the first half process of vacancy migration (right red arrow in **c**) is drawn detailed in **d**. Also note the top-view of the top-row structures

in **d** is rotated with respect to the structures in **c** and that in **Fig**. 1.
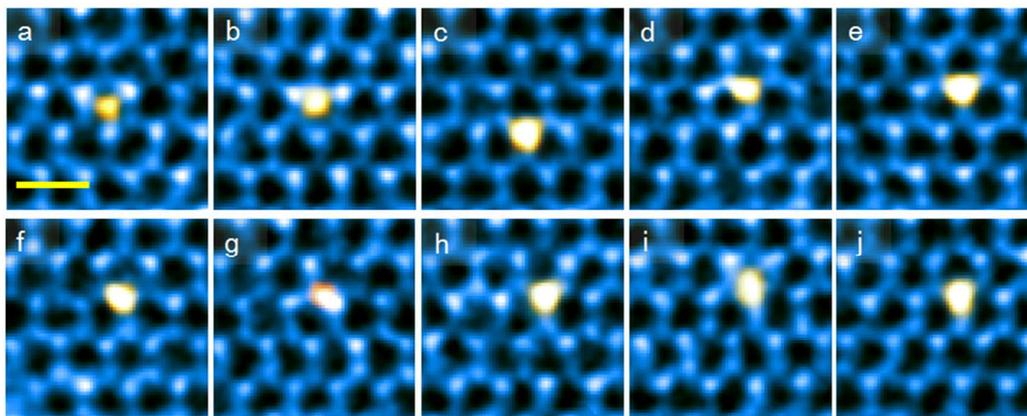
Figure 3. Atomic migration of Mo adatom defects. (**a-j**) Experimental time sequential of ADF images of Mo adatom hopping as an example. Time interval: 3s. Scale bar: 0.5nm. Different false colors are used for better visualization.
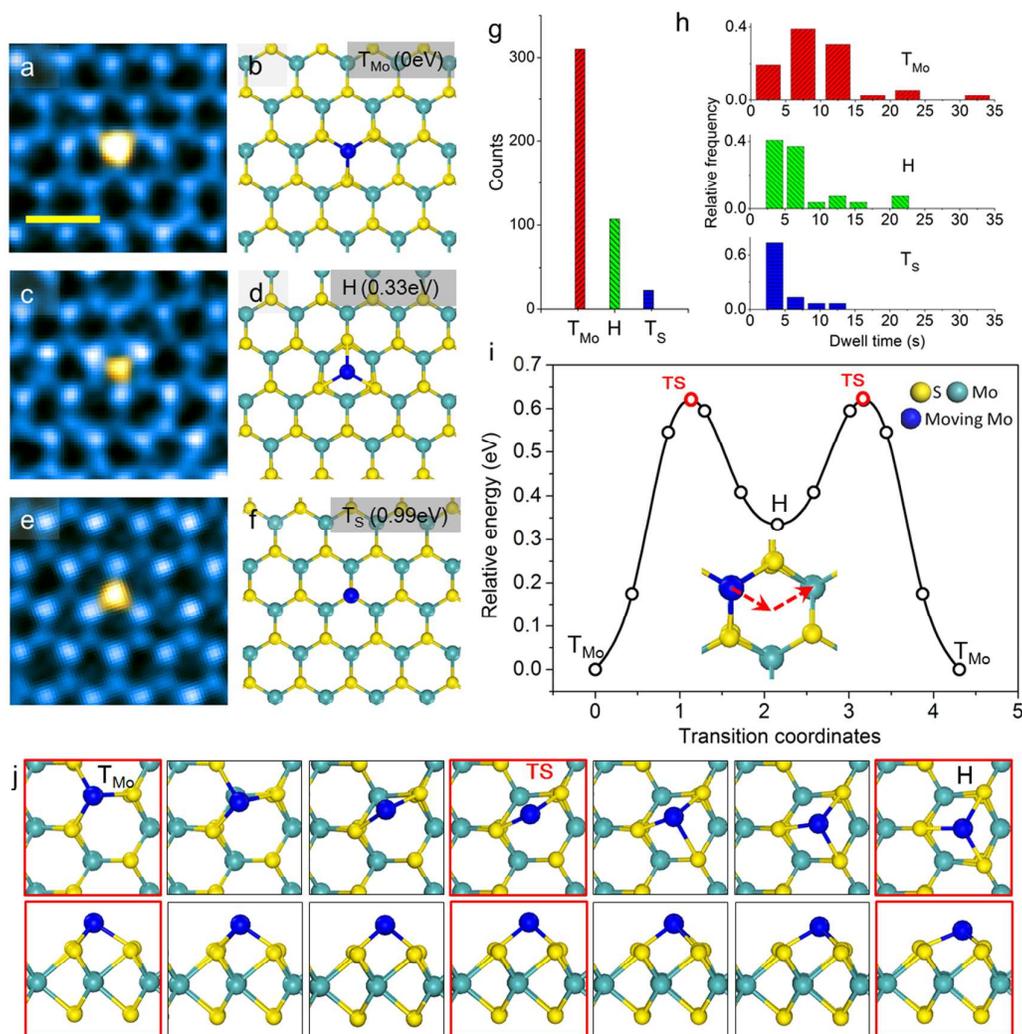
Figure 4. Adsorption states and their evolution along the kinetic pathway. (a-f) Atomically resolved ADF images and structure models of different adsorption states on top of Mo site (T_{Mo}), at hexagon-center or hollow site (H), and on top of S site (T_S), respectively. Scale bar: 0.5nm. False color is used to better illustrate the adatom configuration. Relative energies of different adatom states are given. **(g)** Statistical counts of different adsorption states in **a**,**c**,**e**. **(h)** Statistical dwell time of different adatom structures. **(i)** DFT revealed energetics and pathway for evolution between ground state T_{Mo}, transition state TS, and metastable state H. **(j)** Detailed atomic dynamics of transition from T_{Mo} to H with top view and side view of the three dimensional atomic structure respectively. Note the $T_{Mo1} \rightarrow H \rightarrow T_{Mo2}$ transition in **i** is symmetric, hence only the first half process (left red arrows in **i**) is drawn.
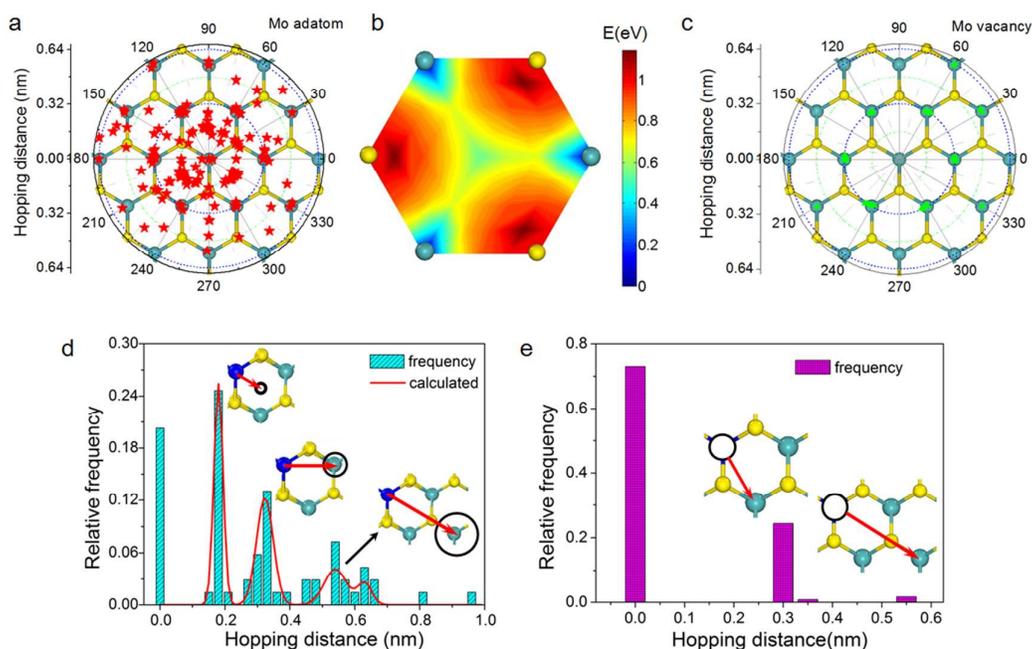
Figure 5. Statistical hopping steps of adatom and vacancy defects. (**a**) Polar scatter diagram of hopping steps from the coordinate origin where Mo lattice locates. Red star dots indicate the final position of adatom hopping from the initial state at the origin. The data is obtained from analyzing over 50 time-series of ADF images of adatom defects on MoS_2 monolayers, (**b**) DFT calculated two-dimensional potential diagram for a Mo adatom on the hexagonal MoS_2 lattice. T_{Mo} sites and hexagon center H site are potential valleys. (**c**) Polar scatter diagram showing hopping steps of Mo vacancy from the origin. (**d**) Hopping step statistics of Mo adatom migration. Insets show the corresponding atomic hopping models which are supported by the calculated probability distribution. (**e**) Hopping step distribution of Mo vacancy with inset models presenting the migration process.
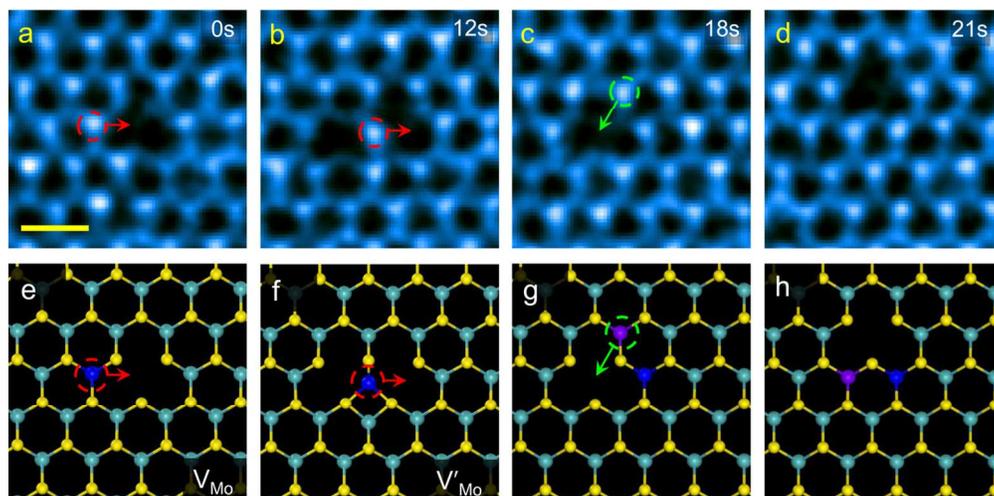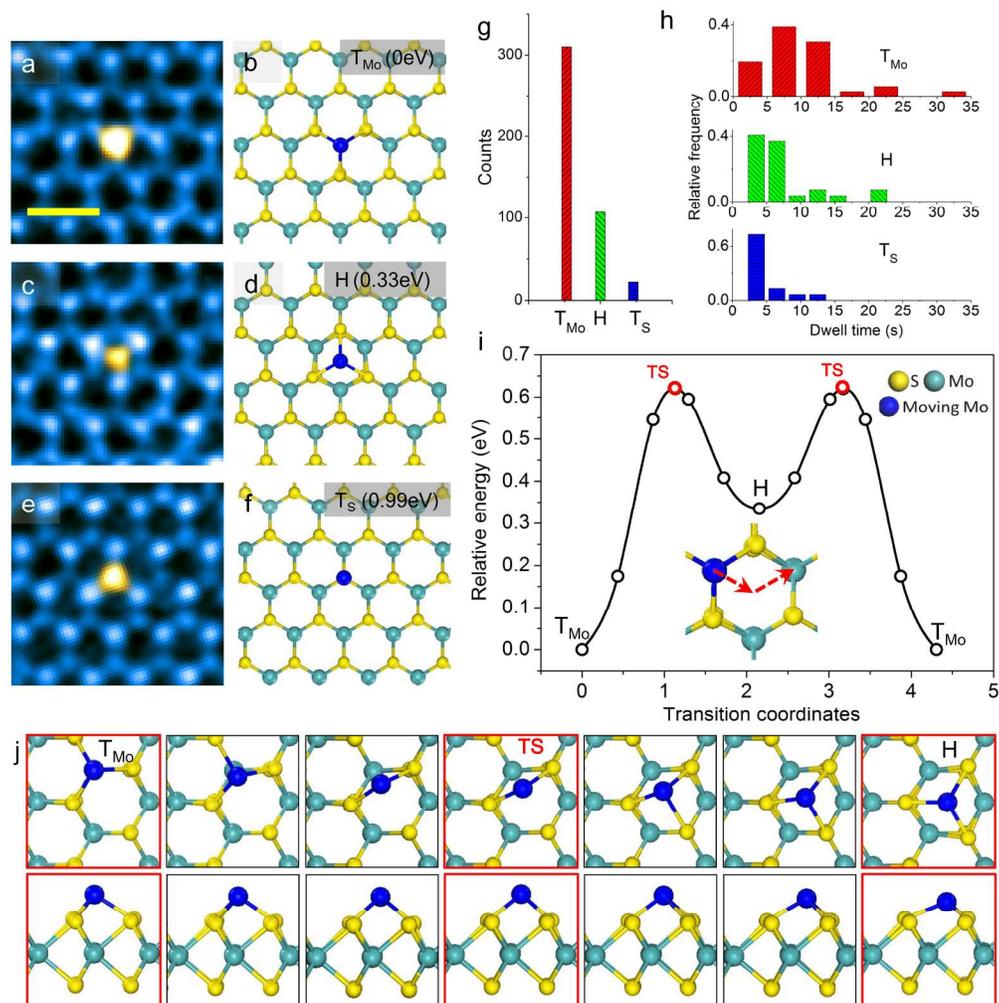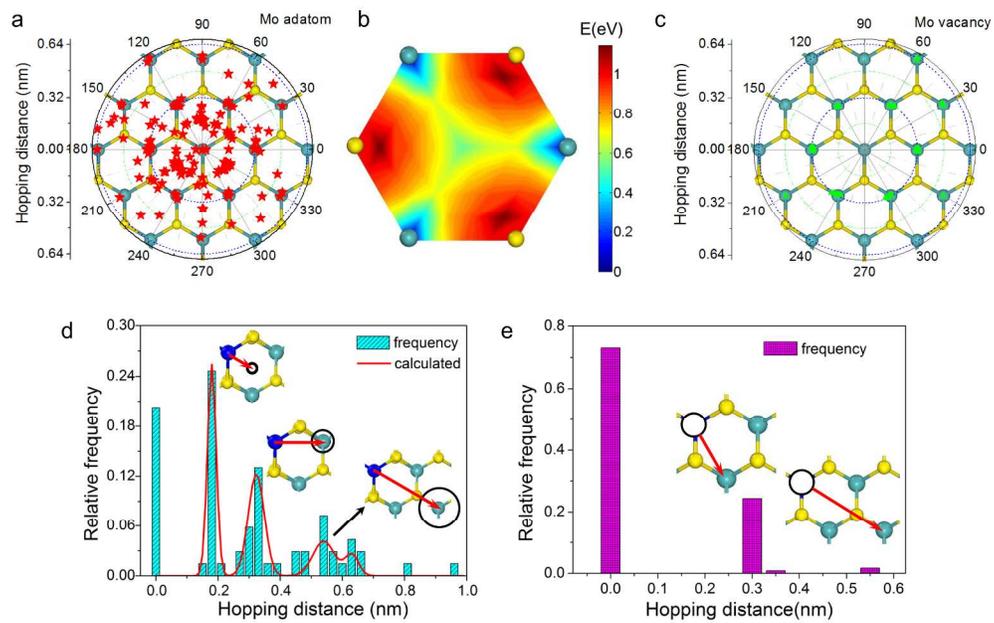
124x61mm (300 x 300 DPI)
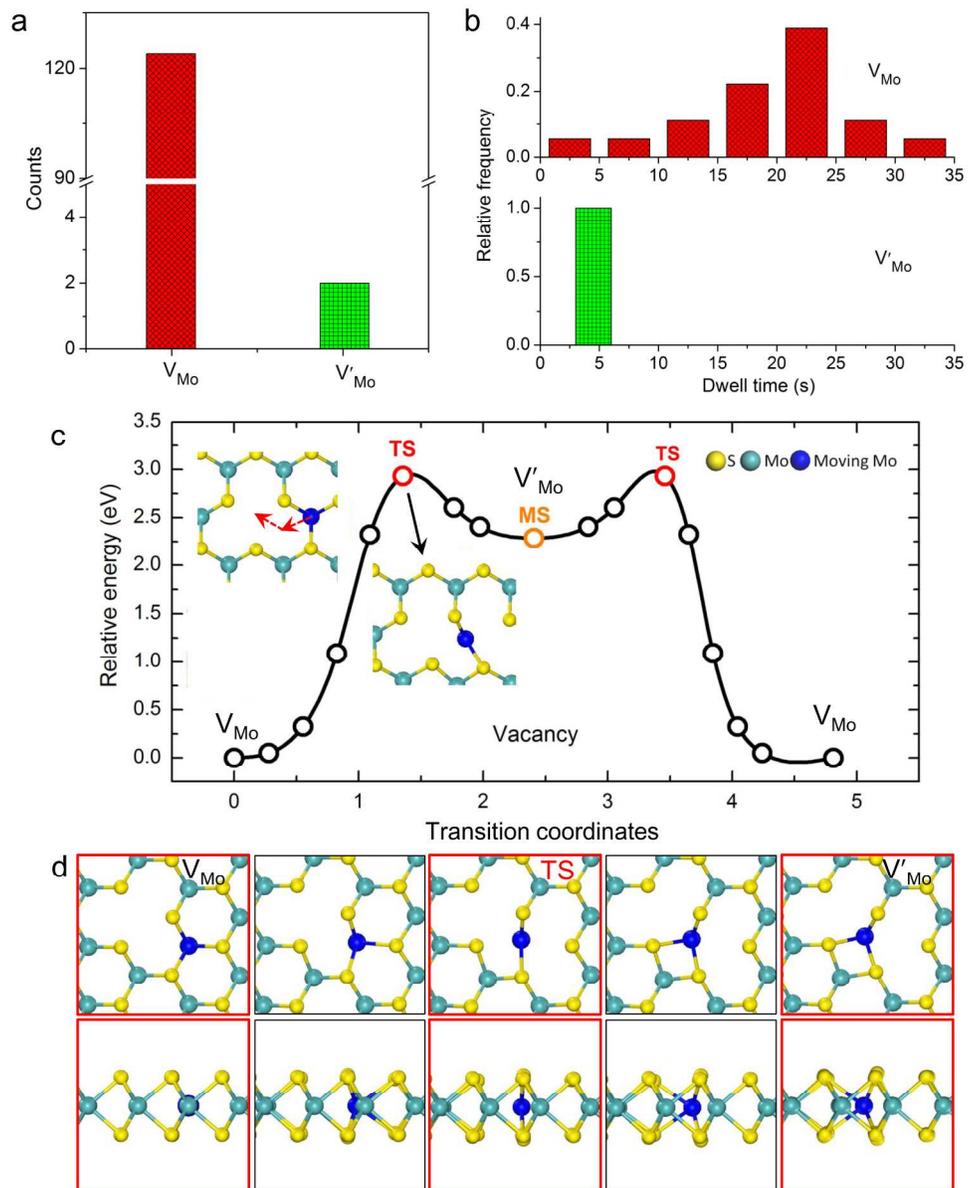
200x247mm (300 x 300 DPI)
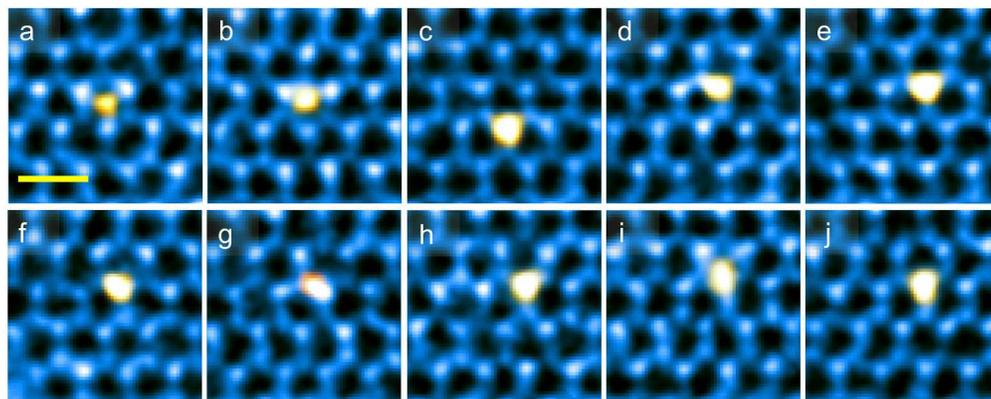
230x92mm (300 x 300 DPI)

230x233mm (300 x 300 DPI)

235x146mm (300 x 300 DPI)